ACS APPLIED MATERIALS & INTERFACES

www.acsami.org Research Article

Hollow Stair-Stepping Spherical High-Entropy Prussian Blue Analogue for High-Rate Sodium Ion Batteries

Yifan Zhang, Jiajia Huang,* Linyang Qiu, Runyu Jiao, Yanhua Zhang, Guozheng Yang, Leiqian Zhang, Zhihong Tian, Elke Debroye, Tianxi Liu, Jean-François Gohy, Johan Hofkens, and Feili Lai*

Cite This: *ACS Appl. Mater. Interfaces* 2024, 16, 27684−27693 Read Online

ACCESS | Metrics & More | Article Recommendations | Supporting Information

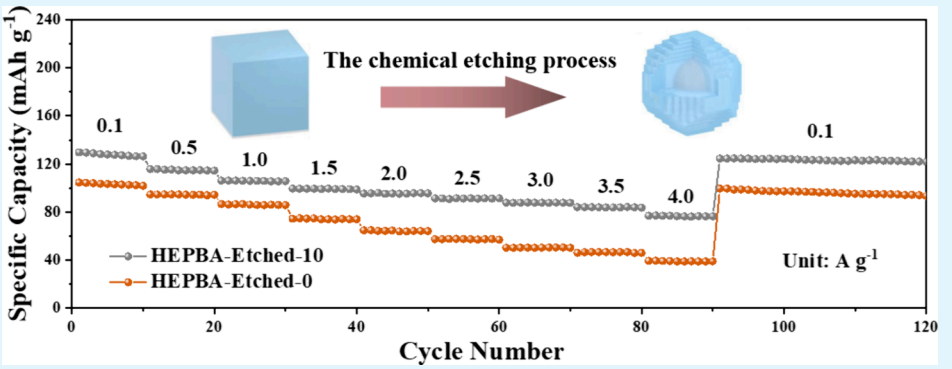

ABSTRACT: Prussian blue analogues (PBAs) are considered to be one of the most suitable sodium storage materials, especially with the introduction of the high-entropy (HE) concept into their structure to further improve their various abilities. However, severe agglomeration of the HEPBA particles still limits the fast charging capabilities. Here, an HEPBA ($Na_x(FeMnCoNiCu)[Fe(CN)_6]_y\square_{1-y}\cdot nH_2O$) with a hollow stair-stepping spherical structure has been prepared through the chemical etching process of the traditional cubic structure of HEPBA. Electrochemical characterization (sodium ion battery), kinetic analysis, and COMSOL Multiphysics simulations reveal that the nature of the high-entropy and the hollow stair-stepping spherical structure can greatly improve the diffusion behavior of Na^+ ions. Moreover, the hollow structure effectively mitigates the volume change of HEPBA during SIBs operation, ultimately extending the lifespan. Consequently, the as-prepared HEPBA cathode exhibits excellent rate performance (126.5 and 76.4 mAh g^{-1} at 0.1 and 4.0 A g^{-1}, respectively) and stable long-term capability (maintaining its 75.6% capacity after 1000 cycles) due to its unique structure. Furthermore, the waste of the etching process can easily be recycled to prepare more HEPBA product. This processing method holds great promise for designing nanostructures of advanced high-entropy Prussian blue analogues for sodium ion batteries.

KEYWORDS: *high-entropy material, Prussian blue analogues, cathode, etching, sodium-ion battery*

INTRODUCTION

The sodium-ion battery (SIB) emerges as a promising alternative to lithium-ion batteries for large-scale electric energy storage (EES) systems, owing to its cost-effectiveness and the widespread availability of sodium resources.[1−3] In order to accommodate the high instantaneous current intensity of input/output in large-scale EES systems, it is crucial to develop ideal cathode materials for SIBs that exhibit exceptional rate performance and long cycle life.[4] Currently, there are four main typical cathode materials for SIBs, including transition metal oxides,[5] phosphate polyanionic compounds,[6] organic compounds,[7] and Prussian blue analogues (PBAs).[8] PBAs are metal hexacyanoferrates with a general formula of $A_xM[Fe(CN)_6]_y\square_{1-y}\cdot nH_2O$ ($0 < x \leq 2$, $0 < y \leq 1$; A, M, and □ represent alkali metal ions, transition metal ions, and $[Fe(CN)_6]^{4-}$ vacancies, respectively; M and Fe are high-spin and low-spin states, respectively).[9] Because of their simple preparation, minimal volume changes during the charge/discharge process, adjustable components, extensive three-dimensional ion diffusion channels, and abundant sodium storage sites, PBAs are regarded as suitable cathode materials for SIBs.[10,11] However, the shortcomings of PBAs include the introduced $[Fe(CN)_6]^{4-}$ vacancies in the crystallization process, coordinated water that is difficult to remove, and the so-called Jahn−Teller effect of Mn-based PBAs, which limit

Received: March 22, 2024
Revised: May 6, 2024
Accepted: May 6, 2024
Published: May 16, 2024

the rate performance and cycle stability of SIBs. Various methods have been put forward to address these issues and promote the practical application of PBAs, such as a postsynthetic and in situ $[Fe(CN)_6]^{4-}$ vacancy repairing strategy,[12] chelating agent-assisted regulation of the crystallization process,[13,14] the modification of electrolyte formulations to promote the involvement of coordination water in the formation of the solid electrolyte interphase structure,[15,16] the construction of core−shell structure to inhibit the structural deformation caused by the Jahn−Teller effect,[17] and dual-metal incorporation strategies in the M site of PBA,[18,19] etc.

Recently, the widespread discovery and reporting of high-entropy (HE) alloys have prompted the development of a variety of single-phase high-entropy materials (HEMs),[20,21] including high-entropy perovskite oxides,[22] high-entropy MXenes,[23] and high-entropy metal organic framework,[24] etc. The design of HEMs typically involves multiple components in approximately equal proportions to achieve a uniform and random distribution. The inherent high configurational entropy system achieved in HEM confers structural stability and superior performance compared with low-entropy and medium-entropy materials. This is attributed to the high-entropy effect and the synergistic "cocktail" effect arising from the mixed presence of multiple cations.[25] Ma and co-workers reported a high-entropy Prussian blue analogue (HEPBA) as an ideal cathode for SIBs,[26] which not only exhibited long-term cycling stability but also excellent rate performance as compared to the corresponding medium-entropy PBAs electrodes. In their follow-up study,[27] they uncovered the rationale behind the improved sodium storage performance of HEPBA: the entropy-mediated mitigation of structural degradation and phase transitions became more pronounced with increasing entropy levels. Lun and co-workers discovered that the disordered permeation network formed by various transition metals in high-entropy cation-disordered rock salt can promote the diffusion of alkali metal ions in the electrode.[28] However, the performance of HEPBAs is still confined, particularly under high current densities (>1 A g^{-1}), which may be caused by the severe agglomeration of large sized HEPBA particles. This self-blocked structure will significantly limit the contact area between the cathode and the electrolyte, thereby inhibiting the diffusion of sodium ions.[29] For traditional single-metal PBAs, various elaborate nanostructures (e.g., nanoflower,[30] dual-textured nanocube,[31] and nanoflake[32]) can be designed and constructed by regulating the crystallization environment to address the issue from the severe agglomeration. As for HEPBAs, however, it remains a huge challenge to maintain nanostructures after incorporating extra metal species.

This study introduces hollow stair-stepping spherical HEPBA, synthesized through a chemical etching process, as a cathode material for SIBs, showcasing remarkable high-rate performance (126.5 and 76.4 mAh g^{-1} at 0.1 and 4.0 A g^{-1}, respectively) and enduring long-term stability (maintaining 75.6% capacity after 1000 cycles). The superior Na^+ storage capabilities of HEPBA stem from its high-entropy composition and unique hollow stair-stepping spherical structure, elucidated through kinetic analyses and COMSOL Multiphysics simulation. Importantly, the recyclability of the etching solution underscores the practical potential of this synthetic approach, allowing for the efficient production of additional HEPBA material.

RESULTS AND DISCUSSION

The etched HEPBA was prepared in two steps, including the synthesis of nanocubic HEPBA ($Na_x(FeMnCoNiCu)[Fe(CN)_6]_y\square_{1-y}\cdot nH_2O$) through a coprecipitation method with five metal cations (Fe, Mn, Co, Ni, and Cu) and subsequent alkaline corrosion process. The influence of OH^- concentration on the morphology of HEPBA was first studied by using etching solutions with varied OH^- concentrations of 0, 1, 10, and 100 mM, which were denoted as HEPBA-Etched-0, HEPBA-Etched-1, HEPBA-Etched-10, and HEPBA-Etched-100, respectively. Due to the insolubility of transition metal hydroxides in an alkaline environment produced by the chemical etching process, the presence of $C_6H_5O_7^{3-}$ species in the etching solution, which can chelate free transition metal ions, is crucial for preventing impurities in the HEPBA. The schematic diagram for the chemical etching process of HEPBA-Etched-0 is shown in Figure 1a, where the OH^- and

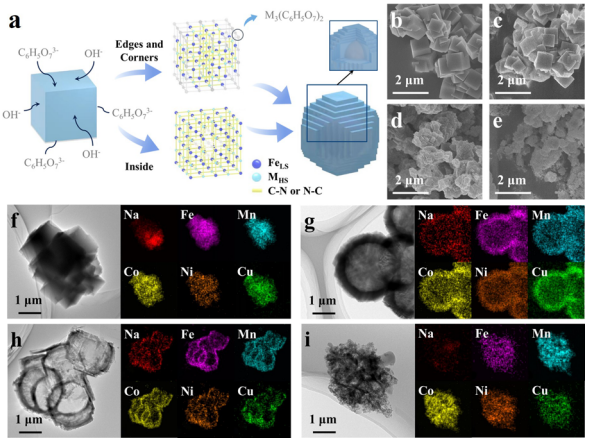

Figure 1. (a) Schematic diagram for the chemical etching process of HEPBA-Etched-0. SEM images of (b) HEPBA-Etched-0, (c) HEPBA-Etched-1, (d) HEPBA-Etched-10, and (e) HEPBA-Etched-100. TEM images and corresponding EDS elemental mappings of (f) HEPBA-Etched-0, (g) HEPBA-Etched-1, (h) HEPBA-Etched-10, and (i) HEPBA-Etched-100.

$C_6H_5O_7^{3-}$ species from the etching solution can remove Fe at low-spin state (Fe_{LS}) and M (Fe, Mn, Co, Ni, and Cu) at high-spin state (M_{HS}) from the lattice of HEPBA into solution,[33] causing changes in morphology of the HEPBA that were recorded through scanning electron microscopy (SEM) and transmission electron microscopy (TEM) images. The HEPBA-Etched-0 particles display uniform cubic shapes with sizes around 500 nm (Figure 1b), attributed to the plentiful presence of sodium citrate in the synthesis process.[34] In contrast, both HEPBA-Etched-1 (Figure 1c) and HEPBA-Etched-10 (Figure 1d) exhibit stepped surfaces and decreased particle sizes. As shown in Figure 1e, however, the three-dimensional structure of HEPBA-Etched-100 is destroyed and collapsed completely at a high OH^- concentration. As compared to the solid structure of HEPBA-Etched-0 (Figure 1f), the HEPBA-Etched-1 (Figure 1g) and HEPBA-Etched-10 (Figure 1h) form cavities with hollow structures, which can be attributed to the internal chemical etching process via the diffused $C_6H_5O_7^{3-}$ and OH^- species.[35,36] Unquestionably, the higher OH^- concentration of HEPBA-Etched-10 leads to a thinner wall than that of HEPBA-Etched-1. The TEM image of HEPBA-Etched-100 confirms its collapsed and agglomerated

https://doi.org/10.1021/acsami.4c04785
ACS Appl. Mater. Interfaces 2024, 16, 27684−27693

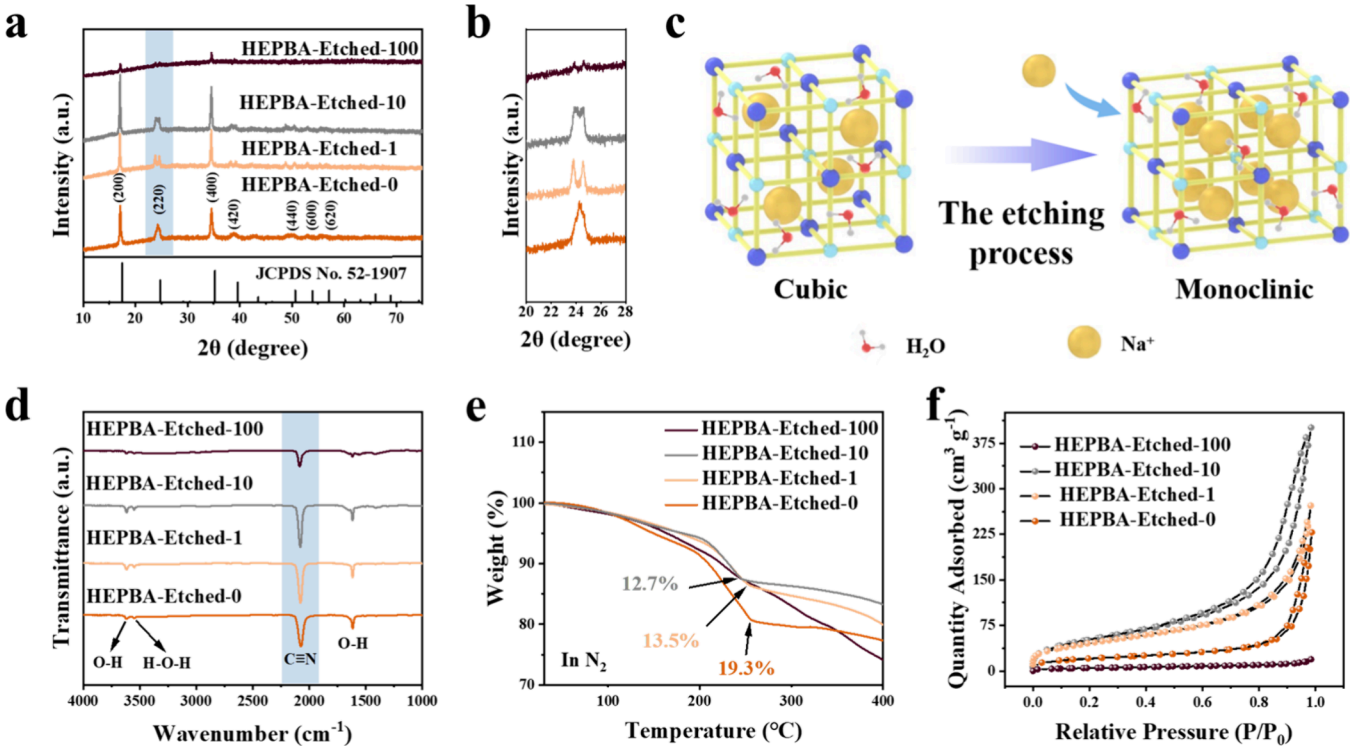

Figure 2. (a) XRD patterns and (b) the corresponding enlarged view at around 24° of HEPBA-Etched-0, HEPBA-Etched-1, HEPBA-Etched-10, and HEPBA-Etched-100. (c) Schematic diagram of crystal phase transformation in the HEPBA lattice during the etching process. (d) FTIR spectra, (e) TGA curves from 25 to 400 °C, and (f) N_2 adsorption−desorption isotherms of HEPBA-Etched-0, HEPBA-Etched-1, HEPBA-Etched-10, and HEPBA-Etched-100.

structure (Figure 1i), which is a result of the excessive etching process under an extra-high OH^- concentration.[33]

The energy dispersive X-ray spectroscopy (EDS) elemental mappings reveal uniform distributions of the five transition metal elements (Fe, Mn, Co, Ni, and Cu) in HEPBA-Etched-0, HEPBA-Etched-1, HEPBA-Etched-10, and HEPBA-Etched-100 (Figure 1f−i). Although the distribution of Na element in HEPBA-Etched-0 is uneven, the etching process results in a more homogeneous distribution of Na element in both the HEPBA-Etched-1 and HEPBA-Etched-10. However, the proportion of Na in HEPBA-Etched-100 decreases significantly (Figure 1i), which can be attributed to the loss of sodium storage sites caused by the chemical etching process.[37] X-ray photoelectron spectroscopy (XPS) was also employed to characterize the existence of Fe, Mn, Co, Ni, and Cu species in HEPBA-Etched-0, HEPBA-Etched-1, HEPBA-Etched-10, and HEPBA-Etched-100 (Figure S1), which demonstrates the negative changes in these five elements under different etching conditions.

Furthermore, X-ray diffraction (XRD) techniques were carried out to observe the influence of the etching process on the crystal structure of HEPBA. The XRD pattern of HEPBA-Etched-0 in Figure 2a exhibits a set of characteristic diffraction peaks typically belonging to PBA. In particular, the peaks at 17.1, 24.2, 34.6, 38.9, 49.9, 52.9, and 55.9° correspond to the (200), (220), (400), (420), (440), (600), and (620) crystal planes (JCPDS No. 52-1907),[38] indicating its single-phase cubic structure. While the HEPBA-Etched-1 and HEPBA-Etched-10 exhibit similar characteristic patterns to HEPBA-Etched-0, their (220) peaks around 24° split into two (Figure 2b), suggesting a phase transition from cubic to monoclinic structures.[39] As for HEPBA-Etched-100, the majority of the characteristic peaks disappear in its XRD pattern, which originates from its completely destroyed PBA structure under a highly concentrated OH^- solution. The sodium storage sites in PBAs synthesized by coprecipitation method are usually not fully occupied by sodium ions, resulting in their cubic structure.[13] However, the empty sodium storage sites can be occupied by the sodium ions in the etching solution gradually, leading to the generation of monoclinic structures in HEPBA-Etched-1 and HEPBA-Etched-10.[40] Therefore, the crystal phase transformation process is considered to be caused by the increased sodium content in the PBA structure (Figure 2c).[41] The results of inductively coupled plasma-optical emission spectroscopy (ICP-OES) shown in Table S1 prove higher sodium contents of HEPBA-Etched-1 and HEPBA-Etched-10 than that of HEPBA-Etched-0, confirming the crystal phase transformation process of HEPBAs.

Fourier transform infrared (FTIR) spectrometry was employed to analyze the effect of chemical etching on the chemical structures of the HEPBAs. As the FTIR spectra of HEPBA-Etched-0, HEPBA-Etched-1, HEPBA-Etched-10, and HEPBA-Etched-100 presented in Figure 2d show, the main absorption peaks at the wavenumbers of 1617, 2074, 3548, and 3616 cm^{-1} correspond to the O−H (interstitial water), C≡N, H−O−H (interstitial water), and O−H (absorbed water) bonds, respectively.[38] Notably, all of the HEPBA contain water molecules, as confirmed by their FTIR spectra, and the thermal gravimetric analysis (TGA) curves in Figure 2e provide the differences in water contents of various HEPBAs. The weight losses between 25 and 210 °C and 210−250 °C can be attributed to the removal of interstitial water and absorbed water, respectively,[42,43] while the subsequent weight loss after

https://doi.org/10.1021/acsami.4c04785
ACS Appl. Mater. Interfaces 2024, 16, 27684−27693

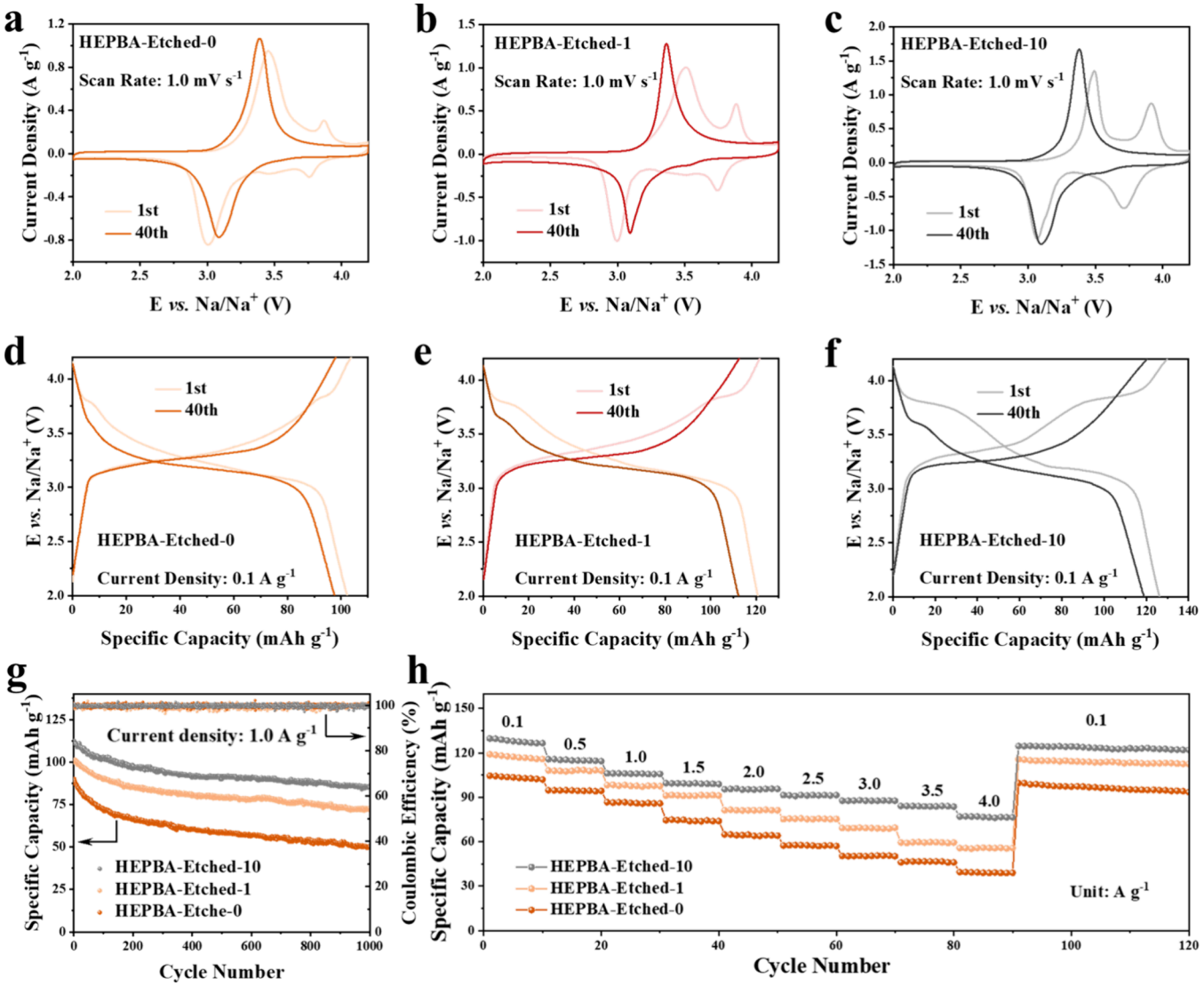

Figure 3. CV curves for the 1st and 40th cycles of (a) HEPBA-Etched-0, (b) HEPBA-Etched-1, and (c) HEPBA-Etched-10 cathodes at 1.0 mV s^{-1}. The galvanostatic charge/discharge curves for the 1st and 40th cycles of (d) HEPBA-Etched-0, (e) HEPBA-Etched-1, and (f) HEPBA-Etched-10 cathodes at 0.1 A g^{-1}. (g) Cycling performance at 1.0 A g^{-1} and (h) rate performance at various current densities.

250 °C can be assigned to the decomposition of HEPBA frameworks (Figure S2).[42] As a result, the water contents of HEPBA-Etched-0, HEPBA-Etched-1, and HEPBA-Etched-10 are 19.3%, 13.5%, and 12.7%, respectively. However, the TGA curve of HPEBA-Etched-100 shows an unrecognizable range for the loss of water, which is due to its poor thermal stability caused by its damaged structure.[44] Based on the TGA curves and ICP-OES results (Table S1), the molecular formulas of HEPBA-Etched-0, HEPBA-Etched-1, and HEPBA-Etched-10 can be confirmed as $Na_{1.335}Fe_{0.207}Mn_{0.197}Co_{0.199}Ni_{0.199}Cu_{0.198}[Fe(CN)_6]_{0.726}\square_{0.274}\cdot 3.198H_2O$, $Na_{1.601}Fe_{0.183}Mn_{0.211}Co_{0.201}Ni_{0.205}Cu_{0.200}[Fe(CN)_6]_{0.930}\square_{0.070}\cdot 2.515H_2O$, and $Na_{1.816}Fe_{0.179}Mn_{0.215}Co_{0.215}Ni_{0.195}Cu_{0.196}[Fe(CN)_6]_{0.964}\square_{0.036}\cdot 2.443H_2O$, respectively, while the formula for HEPBA-Etched-100 cannot be obtained using the same method due to the lack of a defined crystal structure. From the formulas of HEPBA-Etched-0, HEPBA-Etched-1, and HEPBA-Etched-10, it can be observed that the five transition metal elements at the M site are present in almost equal molar amounts with a gradually increased Na content. Furthermore, the ratio of Fe_{LS} to M_{HS} (Fe, Mn, Co, Ni, and Cu) atoms increases slightly from 0.726 in HEPBA-Etched-0 to 0.930 in HEPBA-Etched-1 and 0.964 of HEPBA-Etched-10, which is attributed to the formation of unconventional cation vacancies due to the fact that the OH^- can remove more M_{HS} than Fe_{LS}.[45] As shown in Figure 2f, the Brunauer−Emmett−Teller (BET) specific surface areas of HEPBA-Etched-0, HEPBA-Etched-1, HEPBA-Etched-10, and HEPBA-Etched-100 were measured by nitrogen adsorption−desorption analysis at 77 K, which are 72.3, 164.8, 194.3, and 17.7 m^2 g^{-1}, respectively, suggesting that the cavities formed by the chemical etching process can increase the specific surface area of HEPBAs significantly. It is worth noting that the low specific surface area of HEPBA-Etched-100 originates from its destroyed structure with abundant aggregated nanofragments as can be seen from its TEM image (Figure 1i).[46]

To investigate the effect of hollow stair-stepping spherical morphology on the electrochemical behavior of HEPBAs, various SIBs were assembled by using HEPBA-Etched-0, HEPBA-Etched-1, HEPBA-Etched-10, and HEPBA-Etched-100 as cathodes. Due to the presence of water molecules within the HEPBA lattice (as shown in Figure 2d,e), an electrolyte comprising fluoroethylene carbonate (1.0 M

https://doi.org/10.1021/acsami.4c04785
ACS Appl. Mater. Interfaces 2024, 16, 27684−27693

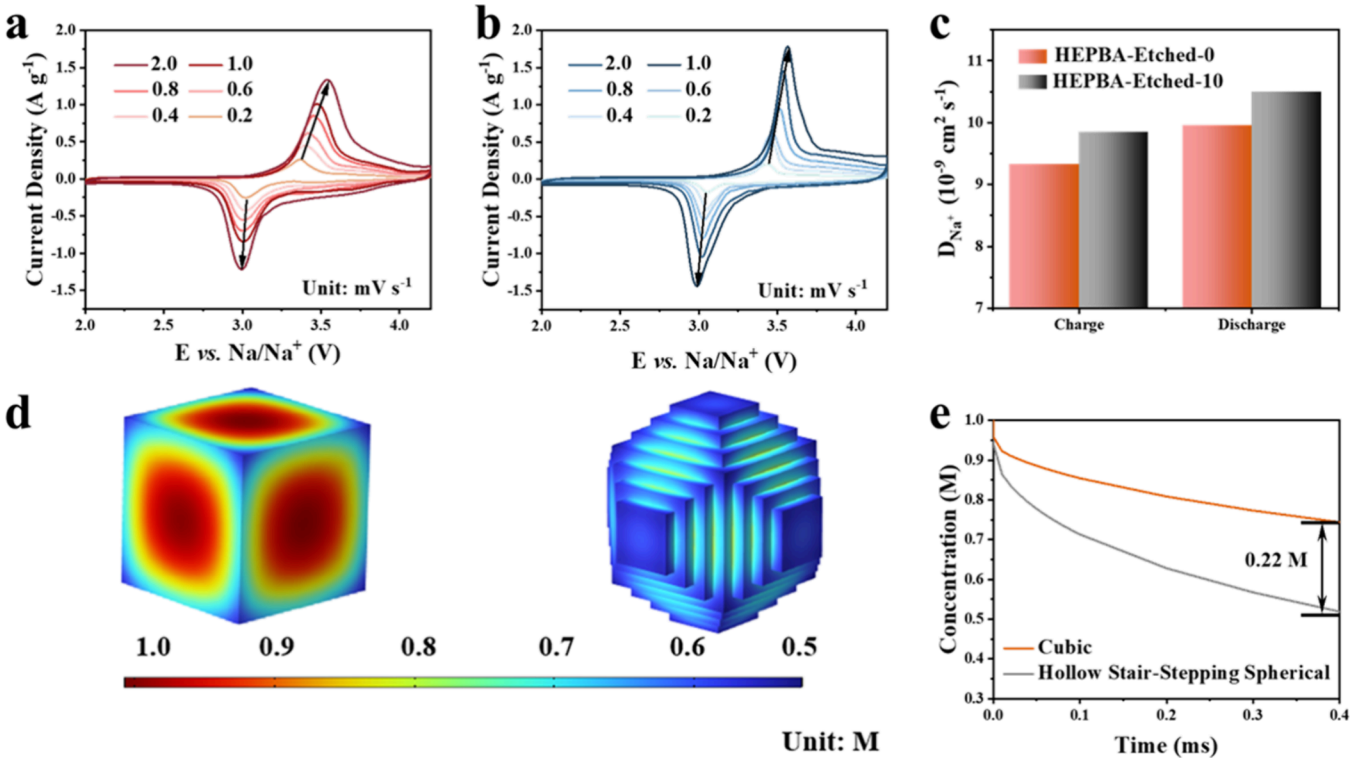

Figure 4. CV curves of (a) HEPBA-Etched-0 and (b) HEPBA-Etched-10 cathodes at different scan rates from 0.2 to 2.0 mV s^{-1}. (c) Na^+ diffusion coefficients of HEPBA-Etched-0 and HEPBA-Etched-10 cathodes during the charge and discharge processes calculated by Randles−Sevcik method. (d) Distributions of Na^+ surface concentration by COMSOL Multiphysics simulation and (e) curves of the Na^+ concentration inside the cubic and hollow stair-stepping spherical models after diffusing of 0.4 ms.

$NaClO_4$ in a 1:1 vol% mixture of ethylene carbonate (EC) and dimethyl carbonate (DMC) with 5.0% fluoroethylene carbonate) was selected. This choice aims to facilitate the involvement of water molecules in the formation of a solid electrolyte interphase (SEI) layer during subsequent electrochemical tests of HEPBAs.[16] The cyclic voltammetry (CV) curves of various SIBs (Figures 3a−c and S3a) illustrate that all of the HEPBAs have two pairs of redox peaks at 3.0/3.5 and 3.7/3.9 V for their initial cycles. When scanning the 40th cycle, the two pairs of redox peaks for HEPBA-Etched-0, HEPBA-Etched-1, and HEPBA-Etched-10 cathodes overlap to form only one pair of redox peaks at 3.1/3.4 V. Although the CV curve of the 40th cycle for HEPBA-Etched-100 cathode still exhibits several redox peaks, there is also a noticeable trend of overlap. Moreover, their corresponding galvanostatic charge/discharge (GCD) curves (Figures 3d−f and S3b) reveal that the voltage plateaus at 3.0/3.5 and 3.7/3.9 V in the first cycle are also replaced by the one at 3.1/3.4 V in the 40th cycle. The merging of redox peaks can be explained by the energy overlap of $M_{HS}^{2+/3+}$ and $Fe_{LS}^{2+/3+}$ couples caused by the water extraction during the cycling.[4,38]

Furthermore, the area of the CV curve of HEPBA-Etched-10 is the largest among the four samples, which indicates its highest specific capacity.[47] In this regard, HEPBA-Etched-0, HEPBA-Etched-1, HEPBA-Etched-10, and HEPBA-Etched-100 deliver capacities of 102.2, 120.7, 126.5, and 43.7 mAh g^{-1}, respectively. The HEPBA-Etched-100 almost loses its electrochemical energy storage property due to the excessive chemical etching process.

The stabilities of the four cathodes were also evaluated by cycling various batteries under a current density of 1.0 A g^{-1} (Figures 3g and S4). As compared with the rapidly declining capacity of the HEPBA-Etched-0 cathode (55.8% capacity retention after 1000 cycles), both the HEPBA-Etched-1 (71.8% capacity retention after 1000 cycles) and HEPBA-Etched-10 cathodes (75.6% capacity retention after 1000 cycles) exhibit remarkable improvement in cycling stability. In contrast, the capacity retention of the cell with the HEPBA-Etched-100 cathode is only 52.3% after 500 cycles. The stable long-term performance of HEPBA-Etched-10 can be attribute to its low water content,[42] and the volume change caused by Na^+ inserting and extracting behaviors can also be alleviated by the hollow structure significantly.[48,49] XPS was also conducted on the HEPBA-Etched-0 and HEPBA-Etched-10 cathodes after 100 cycles to evaluate their reversible performance in energy storage (Figure S5). At the state of complete discharging of SIBs (2.0 V), there is no Fe^{3+} species in both of HEPBAs. Upon charging the SIBs to 4.2 V, the weaker peaks at 709 and 721 eV representing Fe^{2+} indicate that partial Fe^{2+} species are oxidized to Fe^{3+} species in both HEPBA-Etched-0 and HEPBA-Etched-10 cathodes. However, the almost complete transformation toward Fe^{3+} in HEPBA-Etched-10 cathode suggests that there are more available energy storage sites after several cycles.[40]

The rate performance of different HEPBAs-based SIBs was evaluated under various current densities. As shown in Figures 3h and S6, the HEPBA-Etched-10 delivers diminishing specific capacities of 126.5, 114.8, 105.9, 99.5, 95.2, 91.4, 87.7, 83.8, and 76.4 mAh g^{-1} at 0.1, 0.5, 1.0, 1.5, 2.0, 2.5, 3.0, 3.5, and 4.0 A g^{-1}, respectively, which are higher than those of HEPBA-Etched-0 and HEPBA-Etched-1 at corresponding current densities. When the current density recovers to 0.1 A g^{-1}, the capacity of HEPBA-Etched-10 can recover to 124.7 mAh g^{-1}, indicating its excellent rate reversibility. Furthermore, the

https://doi.org/10.1021/acsami.4c04785
ACS Appl. Mater. Interfaces 2024, 16, 27684−27693

capacity retention of HEPBA-Etched-10 (60.4%) at a current density of 4.0 A g^{-1} is much higher than those of HEPBA-Etched-0 (38.0%), HEPBA-Etched-1 (48.1%), and HEPBA-Etched-100 (27.9%). The excellent rate performance observed in HEPBA-Etched-10 underscores the effectiveness of its hollow stair-stepping spherical structure, which offers a high specific surface area. This feature enhances electrochemical performance by providing ample storage sites and shortening diffusion pathways for Na^+ ions, thus accelerating Na^+ diffusion kinetics.[50] Furthermore, the cation vacancies created via the chemical etching process also play a beneficial role in facilitating the extraction and insertion of Na^+ ions.[45] The electrochemical impedance spectroscopy (EIS) plots of HEPBA-Etched-0, HEPBA-Etched-1, HEPBA-Etched-10, and HEPBA-Etched-100 cathodes at 2.0 V (Figure S7) further reveal their differences in charge-transfer resistance, where the cell with the HEPBA-Etched-10 cathode shows the minimum charge-transfer resistance (177 Ω), followed by the cell with the HEPBA-Etched-1 (196 Ω), HEPBA-Etched-0 (209 Ω), and HEPBA-Etched-100 (252 Ω).

The kinetic analyses were conducted through CV curves under different scan rates from 0.2 to 2.0 mV s^{-1} to further study the reaction kinetics. As depicted in Figure 4a,b, the CV curves of HEPBA-Etched-10 exhibit fewer changes in position as scanning rate increases when compared with the HEPBA-Etched-0, demonstrating it suffers a milder polarization at high current density.[38] Furthermore, their diffusion coefficients of Na^+ ions can be evaluated by the Randles−Sevcik method (Figure S8).[51] The diffusion coefficients of D_{Na+} in HEPBA-Etched-10 cathode are 9.85 × 10^{-9} and 10.5 × 10^{-9} cm^2 s^{-1} during the charging and discharging processes (Figure 4c), respectively, which are higher than those of HEPBA-Etched-0 (9.33 × 10^{-9} and 9.95× 10^{-9} cm^2 s^{-1} during the charging and discharging processes, respectively). The galvanostatic intermittent titration technique (GITT) was also applied to evaluate the Na^+ diffusion coefficients. As plotted in Figure S9, during the charging and discharging processes, the D_{Na+} evolutions of the two samples show similar trends. Obviously, the diffusion kinetic of Na^+ ion in HEPBA-Etched-10 cathode is faster than that in HEPBA-Etched-0 cathode.

Additionally, the b-values are calculated based on their multiple CV curves at different scan rates. As shown in Figure S10, the *b*-values of HEPBA-Etched-0 and HEPBA-Etched-10 are located within the range of 0.5−1 and close to 1, indicating their pseudocapacitive properties as cathodes for SIBs. The capacitive and diffusion contributions of the HEPBA-Etched-0 and HEPBA-Etched-10 cathodes were further quantified (Figure S11).[52] For the HEPBA-Etched-10 cathode, the capacitive contribution increases from 63% at a scan rate of 0.2 mV s^{-1} to 89% at a scan rate of 2.0 mV s^{-1}, surpassing the values observed for the HEPBA-Etched-0 cathode (53% and 75% at 0.2 and 2.0 mV s^{-1}, respectively). The higher proportion capacitive contributions in HEPBA-Etched-10 cathode demonstrate its faster charge/discharge tolerance, resulting in its outstanding rate performance.

COMSOL Multiphysics simulations were conducted to demonstrate the superiority of the hollow stair-stepping spherical morphology of HEPBA-Etched-10. First, cubic and hollow stair-stepping spherical models were established based on the TEM images (Figure 1f,h) with corresponding geometric constructions shown in Figure S12, while the initial Na^+ concentration (1.0 M) and diffusion coefficient of Na^+ ions were the same in two models. Since the Na^+ ion can only contact with the surface in the cubic model, the internal surface in the hollow stair-stepping spherical model can provide additional pathways for the diffusion of Na^+ ions. Furthermore, the average distance for Na^+ diffusion can be shortened greatly due to the thin wall of the hollow stair-stepping spherical model. As a result, the left concentration of Na^+ ions in the hollow stair-stepping spherical model (0.52 M) is lower than that in cubic model (0.74 M) after undergoing diffusion for 0.4 ms (Figure 4d,e). Therefore, both the COMSOL simulations and experimental results (Figure 4c) jointly suggest that the hollow stair-stepping spherical structure can improve the efficiency of Na^+ diffusion.

Interestingly, the chemical etching process would cause serious losses of transition metal ions from the HEPBA framework.[45] Hence, the etching solution was collected and neutralized with citric acid, which was used as a new precursor solution to prepare the resynthesized HEPBA (RE-HEPBA). The RE-HEPBA was also characterized through SEM image, XRD pattern, TGA curve, GCD curves, and ICP-OES. The SEM image of RE-HEPBA (Figure S13) also presents relatively regular cubic shapes with a particle size of ∼ 500 nm, which is similar to the HEPBA-Etched-0. However, there are some agglomerated cubic particles, which is due to the presence of a high concentration of sodium citrate in the neutralized etching solution.[53] The XRD pattern of RE-HEPBA also exhibits sharp and complete PBA characteristic diffraction peaks (Figure S14a), which indicates that the collected etching solution can also be used for the synthesis of HEPBA. Furthermore, the water content of RE-HEPBA is 17.8% (Figure S14b), which is slightly lower than that of HEPBA-Etched-0 (19.3%). The ICP-OES (Table S1) results also indicate that RE-HEPBA has a similar chemical composition ($Na_{1.518}Fe_{0.207}Mn_{0.197}Co_{0.196}Ni_{0.201}Cu_{0.199}[Fe(CN)_6]_{0.744}\square_{0.256}\cdot 2.994H_2O$), which leads to a consistent sodium storage capacity (106.9 mAh g^{-1} at 0.1 A g^{-1}) with HEPBA-Etched-0 (102.2 mAh g^{-1} at 0.1 A g^{-1}) (Figure S15).

CONCLUSION

In summary, we have successfully synthesized an etched high-entropy Prussian blue analogue (HEPBA) cathode material for sodium-ion batteries (SIBs) featuring a hollow stair-stepping spherical morphology via a chemical etching process. Our kinetic analyses and COMSOL simulations reveal that the high-entropy structure, combined with the unique morphology, not only enhances the surface area available for Na^+ ion diffusion but also significantly reduces the average distance for Na^+ diffusion, thereby improving the Na^+ diffusion kinetics. Consequently, the HEPBA cathode demonstrates outstanding rate performance (126.5 and 76.4 mAh g^{-1} at current densities of 0.1 and 4.0 A g^{-1}, respectively). Additionally, the hollow structure alleviates the volume change of HEPBA during the SIBs operation, leading to a stable cycling performance of the HEPBA cathode with a capacity retention of 75.6% after 1000 cycles. This study presents a promising approach for the structural design of high-entropy Prussian blue analogues, offering new insights into the development of advanced SIB cathode materials.

EXPERIMENTAL SECTION

Materials and Chemicals. $FeSO_4\cdot 7H_2O$, $MnSO_4\cdot H_2O$, $NiSO_4\cdot 6H_2O$, $CuCl_2\cdot 2H_2O$, $Na_4[Fe(CN)_6]\cdot 10H_2O$, and *N*-methyl-2-pyrrolidinone (NMP, 99.5%) were purchased from Shanghai Aladdin Biochemical Technology Co., Ltd. $(CH_3COO)_2Co\cdot 4H_2O$, NaOH,

https://doi.org/10.1021/acsami.4c04785
ACS Appl. Mater. Interfaces 2024, 16, 27684−27693

and $C_6H_5Na_3O_7{\cdot}2H_2O$ were purchased from Shanghai Macklin Biochemical Co., Ltd. Sodium metal and electrolyte (1.0 M $NaClO_4$ in ethylene carbonate (EC):dimethyl carbonate (DMC) = 1:1 vol % with 5.0% fluoroethylene carbonate) were purchased from Guangdong Canrd New Energy Technology Co., Ltd.

Synthesis of High-Entropy Prussian Blue Analogue (HEPBA). HEPBA was synthesized by a coprecipitation method. In detail, 1 mmol of each of the five transition metal salts ($FeSO_4{\cdot}7H_2O$, $MnSO_4{\cdot}H_2O$, $(CH_3COO)_2Co{\cdot}4H_2O$, $NiSO_4{\cdot}6H_2O$, and $CuCl_2{\cdot}2H_2O$) and 20 mmol of sodium citrate ($C_6H_5Na_3O_7{\cdot}2H_2O$) were dissolved into 100 mL of deionized water to prepare solution A. Then, 6 mmol of sodium ferrocyanide ($Na_4[Fe(CN)_6]{\cdot}10H_2O$) and 20 mmol of sodium citrate were dissolved into 100 mL of deionized water to prepare solution B. After that, solution A was added to solution B under magnetic stirring slowly, and maintained for 2 h. After being aged at room temperature for 24 h, the obtained solid product was collected by centrifugation, washed with deionized water and ethanol alternately, and dried in a vacuum oven at 80 °C for 24 h.

Synthesis of HEPBA Etched by Solutions with OH^- Concentrations of 0, 1, 10, and 100 mmol L^{-1} (HEPBA-Etched-0, HEPBA-Etched-1, HEPBA-Etched-10, and HEPBA-Etched-100). Except for 20 mmol of sodium citrate in 100 mL of deionized water, the etching solutions for HEPBA-Etched-0, HEPBA-Etched-1, HEPBA-Etched-10, and HEPBA-Etched-100 also contain 0, 1, 10, and 100 mM of NaOH, respectively. Subsequently, 400 mg of HEPBA was dispersed in 100 mL of etching solution under magnetic stirring condition. After keeping for 20 min in the etching solution, the remaining solid was collected by centrifugation, washed with deionized water and ethanol alternately, and dried in a vacuum oven at 80 °C for 24 h.

Synthesis of Resynthesized HEPBA (RE-HEPBA). Centrifugation was used to collect the remaining solution after the chemical etching process of HEPBA-Etched-10. Moreover, the citric acid aqueous solution (1.0 M) was added under magnetic stirring to the above solution until it became neutral, which is named solution A. 100 mL of solution containing 6 mmol of sodium ferrocyanide and 20 mmol of sodium citrate was prepared as solution B. After that, 100 mL of solution A was added to 100 mL of solution B under magnetic stirring slowly and maintained for 2 h. The obtained solid product was obtained by centrifugation, washed with deionized water and ethanol alternately, and dried in a vacuum oven at 80 °C for 24 h.

Characterizations. Scanning electron microscopy (SEM, Jeol JSM-7610FPlus) and transmission electron microscopy (TEM, FEI Tecnai G2 F20 X-Twin) were used to observe the morphology. Energy dispersive spectroscopy (EDS, Oxford ULTIM MAX 40) was used to observe the distribution of the elements. X-ray photoelectron spectrometry (XPS, Shimadzu AXIS SUPRA+) was used to characterize the elemental compositions in the HEPBAs. The binding energies obtained in the XPS spectral analysis were corrected by referencing C 1s to 284.8 eV. The crystal structures were recorded by the Empyrean X-ray diffraction system (XRD) with radiation from a Cu target (λ = 0.154 nm) operating at 45 kV and 40 mA. The contents of various elements in the four HEPBAs were determined by inductively coupled plasma-optical emission spectroscopy (ICP-OES, Agilent 5110). The vibrational state of functional groups was analyzed by Fourier transform infrared spectroscopy (FTIR, Bruker VERTEX 70v). The water content of HEPBA was determined by thermal gravimetric analysis (TGA, NETZSCH STA 2500 simultaneous thermal analyzer) in nitrogen atmosphere, with a heating rate of 10 °C min^{-1} from 25 to 1000 °C. The specific surface areas were measured by nitrogen adsorption−desorption analysis at 77 K and calculated by the Brunauer−Emmett−Teller (BET) method.

Electrochemical Characterizations. Typically, the active material, Ketjen black, and poly(vinylidene fluoride) (PVDF) were mixed with a weight ratio of 7:2:1, by grounding them in an agate mortar with an appropriate amount of *N*-methyl pyrrolidinone (NMP). The electrode was prepared by coating slurry onto carbon paper with the active material of ~2 mg cm^{-2} and drying in a vacuum oven at 120 °C for 24 h. The CR2032-type coin cells were assembled in an argon filled glovebox by using Whatman GF/A glass fiber as the separator, 1 M $NaClO_4$ in ethylene carbonate (EC):dimethyl carbonate (DMC) = 1:1 vol % with 5.0% fluoroethylene carbonate as the electrolyte, and sodium metal as the anode. CHI660E electrochemical test station was used for recording the cyclic voltammetry (CV) curves, electrochemical impedance spectroscopy (EIS) plots, and the galvanostatic intermittent titration technique (GITT). The galvanostatic charge/discharge (GCD) curves and rate capability were performed by a Land CT2001A electrochemical system.

Calculation Method of *b*-Value. The *b*-values were obtained by fitting curve using the logarithm of the peak current densities in the CV curves at different scan rates and the logarithm of the corresponding scan rates, where the slope of the fitted line represents the value of *b* as the following formula:[S1]

$$i_p = av^b$$

where i_p and v are the peak current density (A g^{-1}) and corresponding scan rate (mV s^{-1}), respectively, and a and b are related to adjustable values.

Calculation of Na^+ Diffusion Coefficients through CV Curves (Randles−Sevcik Method). The diffusion coefficient value (D) can be calculated from the following formula:[S4]

$$i_p = (2.69 \times 10^5)n^{3/2}AD^{1/2}Cv^{1/2}$$

where i_p is the peak current density (A g^{-1}), n is the number of electrons per molecule during the intercalation, A is the surface area of the cathode (cm^2), C is the concentration of Na^+ in the electrode (mol cm^{-3}), and v is the corresponding scan rate (V s^{-1}).

Calculation of Na^+ Diffusion Coefficients through GITT Results. The diffusion coefficient (D_{GITT}) value can be calculated from the following formula:[S5]

$$D_{GITT} = 4/\pi\tau(m_BV_M/M_BS)^2(\Delta E_S/\Delta E_\tau)^2$$

where τ is the constant current pulse time (600 s), m_B, V_M, M_B, and S are the mass, molar volume, molar mass, and electrode−electrolyte interface area of HEPBAs, respectively, ΔE_S is the voltage difference during the open circuit period, and ΔE_τ is the total change of cell voltage during a constant current pulse excluding the IR drop.

Quantitative Method of the Capacitive (k_1v) and Diffusion Contributions ($k_2v^{1/2}$) for the Cathode. The capacitive and diffusion contributions can be quantified from the following formula:[S2]

$$i_p = k_1v + k_2v^{1/2}$$

where i_p is the peak current density (A g^{-1}), and v is the corresponding scan rate (V s^{-1}).

COMSOL Multiphysics Simulations. As shown in Figure S12, three-dimensional cubic and hollow stair-stepping spherical models were established with evenly distributed and fixed Na^+ concentrations (1.0 M) based on COMSOL Multiphysics software 6.1. The "tertiary current distribution" interface was selected to describe the current and potential distributions in the cell. The Butler−Volmer equations were used for the reaction kinetics at the electrodes, and Fick's law was used for the mass transport to analyze the transport of Na^+ ions in the cathode.[S6] Besides, the commercial direct solver (package PARDISO, COMSOL Multiphysics) was used to track the changes in concentration for Na^+ ions during their extraction.

■ ASSOCIATED CONTENT

Supporting Information

The Supporting Information is available free of charge at https://pubs.acs.org/doi/10.1021/acsami.4c04785.

XPS spectra, TGA curves, XRD patterns, SEM image, ICP results, CV curves, GCD plots, cycling performance, rate performance, Nyquist plots, GITT results, quantitative capacitive contributions, and the 3D geometric

https://doi.org/10.1021/acsami.4c04785
ACS Appl. Mater. Interfaces 2024, 16, 27684−27693

constructions of COMSOL Multiphysics simulation for samples (PDF)

AUTHOR INFORMATION

Corresponding Authors

Jiajia Huang − *School of Chemical Engineering, Zhengzhou University, Zhengzhou 450001, P. R. China*; Email: huangjiajia@zzu.edu.cn

Feili Lai − *State Key Laboratory of Metal Matrix Composites, School of Materials Science and Engineering, Shanghai Jiao Tong University, Shanghai 200240, P. R. China; Department of Chemistry, KU Leuven, Leuven 3001, Belgium;* orcid.org/0000-0002-4945-0737; Email: feili.lai@kuleuven.be, feililai@sjtu.edu.cn

Authors

Yifan Zhang − *School of Chemical Engineering, Zhengzhou University, Zhengzhou 450001, P. R. China*

Linyang Qiu − *School of Chemical Engineering, Zhengzhou University, Zhengzhou 450001, P. R. China*

Runyu Jiao − *School of Chemical Engineering, Zhengzhou University, Zhengzhou 450001, P. R. China*

Yanhua Zhang − *School of Chemical Engineering, Zhengzhou University, Zhengzhou 450001, P. R. China*

Guozheng Yang − *State Key Laboratory of Metal Matrix Composites, School of Materials Science and Engineering, Shanghai Jiao Tong University, Shanghai 200240, P. R. China*

Leiqian Zhang − *The Key Laboratory of Synthetic and Biological Colloids, Ministry of Education, School of Chemical and Material Engineering, Jiangnan University, Wuxi 214122, P. R. China*

Zhihong Tian − *Engineering Research Center for Nanomaterials, Henan University, Kaifeng 475004, P. R. China*

Elke Debroye − *Department of Chemistry, KU Leuven, Leuven 3001, Belgium;* orcid.org/0000-0003-1087-4759

Tianxi Liu − *The Key Laboratory of Synthetic and Biological Colloids, Ministry of Education, School of Chemical and Material Engineering, Jiangnan University, Wuxi 214122, P. R. China*

Jean-François Gohy − *Institute for Condensed Matter and Nanosciences (IMCN), Bio- and Soft Matter (BSMA), Université Catholique de Louvain (UCL), 1348 Louvain-la-Neuve, Belgium;* orcid.org/0000-0003-4169-1883

Johan Hofkens − *Department of Chemistry, KU Leuven, Leuven 3001, Belgium; Department of Molecular Spectroscopy, Max Planck Institute for Polymer Research, Mainz 55128, Germany;* orcid.org/0000-0002-9101-0567

Complete contact information is available at: https://pubs.acs.org/10.1021/acsami.4c04785

Notes

The authors declare no competing financial interest.

ACKNOWLEDGMENTS

The authors sincerely acknowledge financial support from the National Natural Science Foundation of China (Grants 51873198, 52161135302, and 52211530489) and the Research Foundation-Flanders (FWO, Grants G0F2322N, 1298323N, VS06523N, and V404923N). Thanks are extended to the help of Center of Advanced Analysis & Computational Science of Zhengzhou University for the reported the characterization. F.L. acknowledges the "Xiaomi Young Scholars" program. J.H. acknowledges financial support from the Flemish Government (Moonshot cSBO Project P2C HBC.2019.0108). E.D. acknowledges the European Research Council (ERC Starting Grant 101117274 X-PECT) and the KU Leuven Internal Funds (Grants STG/21/010, C14/23/090, and CELSA/23/018).

REFERENCES

(1) Chen, M.; Liu, Q.; Wang, S.; Wang, E.; Guo, X.; Chou, S. High-Abundance and Low-Cost Metal-Based Cathode Materials for Sodium-Ion Batteries: Problems, Progress, and Key Technologies. *Adv. Energy Mater.* **2019**, *9*, 1803609.

(2) Nayak, P. K.; Yang, L.; Brehm, W.; Adelhelm, P. From Lithium-Ion to Sodium-Ion Batteries: Advantages, Challenges, and Surprises. *Angew. Chem., Int. Ed.* **2018**, *57*, 102−120.

(3) Kundu, D.; Talaie, E.; Duffort, V.; Nazar, L. F. The Emerging Chemistry of Sodium Ion Batteries for Electrochemical Energy Storage. *Angew. Chem., Int. Ed.* **2015**, *54*, 3431−3448.

(4) Zhou, A.; Cheng, W.; Wang, W.; Zhao, Q.; Xie, J.; Zhang, W.; Gao, H.; Xue, L.; Li, J. Hexacyanoferrate-Type Prussian Blue Analogs: Principles and Advances Toward High-Performance Sodium and Potassium Ion Batteries. *Adv. Energy Mater.* **2021**, *11*, 2000943.

(5) Su, H.; Jaffer, S.; Yu, H. Transition Mmetal Oxides for Sodium-Ion Batteries. *Energy Storage Mater.* **2016**, *5*, 116−131.

(6) Zhang, X.; Rui, X.; Chen, D.; Tan, H.; Yang, D.; Huang, S.; Yu, Y. $Na_3V_2(PO_4)_3$: An Advanced Cathode for Sodium-Ion Batteries. *Nanoscale* **2019**, *11*, 2556−2576.

(7) Wu, Y.; Zeng, R.; Nan, J.; Shu, D.; Qiu, Y.; Chou, S. Quinone Electrode Materials for Rechargeable Lithium/Sodium Ion Batteries. *Adv. Energy Mater.* **2017**, *7*, 1700278.

(8) Qian, J.; Wu, C.; Cao, Y.; Ma, Z.; Huang, Y.; Ai, X.; Yang, H. Prussian Blue Cathode Materials for Sodium-Ion Batteries and Other Ion Batteries. *Adv. Energy Mater.* **2018**, *8*, 1702619.

(9) Sun, J.; Ye, H.; Oh, J. A. S.; Plewa, A.; Sun, Y.; Wu, T.; Sun, Q.; Zeng, K.; Lu, L. Elevating the Discharge Plateau of Prussian Blue Analogs Through Low-Spin Fe Redox Induced Intercalation Pseudocapacitance. *Energy Storage Mater.* **2021**, *43*, 182−189.

(10) Sun, R.; You, Y. Prussian White Cathode Materials for All-Climate Sodium-Ion Batteries. *ACS Appl. Mater. Inter.* **2023**, *15*, 44599−44606.

(11) Zhang, Y.; Zhou, X.; Yang, C.; Liu, X.; Wang, M.; Han, J.; Yan, H.; You, Y. Air-Stable Prussian White Cathode Materials for Sodium-Ion Batteries Enabled by ZnO Surface Modification. *ACS Appl. Mater. Inter.* **2024**, *16*, 15649−15656.

(12) Wan, M.; Zeng, R.; Meng, J.; Cheng, Z.; Chen, W.; Peng, J.; Zhang, W.; Huang, Y. Post-Synthetic and In Situ Vacancy Repairing of Iron Hexacyanoferrate Toward Highly Stable Cathodes for Sodium-Ion Batteries. *Nano-Micro Lett.* **2022**, *14*, 9.

(13) Wu, X.; Wu, C.; Wei, C.; Hu, L.; Qian, J.; Cao, Y.; Ai, X.; Wang, J.; Yang, H. Highly Crystallized $Na_2CoFe(CN)_6$ with Suppressed Lattice Defects as Superior Cathode Material for Sodium-Ion Batteries. *Acs Appl. Mater. Inter.* **2016**, *8*, 5393−5399.

(14) Rehman, R.; Peng, J.; Yi, H.; Shen, Y.; Yin, J.; Li, C.; Fang, C.; Li, Q.; Han, J. Highly Crystalline Nickel Hexacyanoferrate as a Long-Life Cathode Material for Sodium-Ion Batteries. *RSC Adv.* **2020**, *10*, 27033−27041.

(15) Luo, Y.; Yang, L.; Liu, Q.; Yan, Y. In Situ Polyaniline Coating of Prussian Blue as Cathode Material for Sodium-Ion Battery. *R. Soc. Open Sci.* **2021**, *8*, 211092.

(16) Thieu, Q. Q. V.; Hoang, H.; Le, V. T.; Nguyen, V. H.; Nguyen, D. Q.; Nguyen, V. D.; Le, M. L. P.; Tran, N. H. T.; Kim, I. T.; Nguyen, T. L. Enhancing Electrochemical Performance of Sodium Prussian Blue Cathodes for Sodium-Ion Batteries via Optimizing Alkyl Carbonate Electrolytes. *Ceram. Int.* **2021**, *47*, 30164−30171.

(17) Gebert, F.; Cortie, D. L.; Bouwer, J. C.; Wang, W.; Yan, Z.; Dou, S.; Chou, S. Epitaxial Nickel Ferrocyanide Stabilizes Jahn-Teller Distortions of Manganese Ferrocyanide for Sodium-Ion Batteries. *Angew. Chem., Int. Ed.* **2021**, *60*, 18519−18526.
(18) Fan, L.; Shu, G.; Liu, Y.; Yu, H.; Yan, L.; Zhang, L.; Shu, J. Cu-Substituted Nickel Hexacyanoferrate with Tunable Reaction Potentials for Superior Ammonium Ion Storage. *J. Mater. Sci. Technol.* **2024**, *169*, 19−27.
(19) Wang, J.; Qiu, C.; Zhao, S.; Guan, M.; Yu, H.; Chen, Z.; Lu, B.; Wanyan, B.; Zhang, L.; Shu, J. Ultra-Stable Cu-Ion-Exchanged Cobalt Hexacyanoferrate(ii) in Aqueous Copper-Ion Storage. *Inorg. Chem. Front.* **2024**, *11*, 1108−1116.
(20) Huang, H.; Zhao, J.; Guo, H.; Weng, B.; Zhang, H.; Saha, R. A.; Zhang, M.; Lai, F.; Zhou, Y.; Juan, R. Z.; Chen, P; Wang, S; Steele, J. A.; Zhong, F.; Liu, T.; Hofkens, J.; Zheng, Y.; Long, J.; Roeffaers, M. B. J. Noble-Metal-Free High-Entropy Alloy Nanoparticles for Efficient Solar-Driven Photocatalytic CO_2 Reduction. *Adv. Mater.* **2024**, 2313209.
(21) Li, Z.; Pradeep, K. G.; Deng, Y.; Raabe, D.; Tasan, C. C. Metastable High-Entropy Dual-Phase Alloys Overcome the Strength-Ductility Trade-Off. *Nature* **2016**, *534*, 227−230.
(22) Chu, K.; Qin, J.; Zhu, H.; De Ras, M.; Wang, C.; Xiong, L.; Zhang, L.; Zhang, N.; Martens, J. A.; Hofkens, J.; Lai, F.; Liu, T. High-Entropy Perovskite Oxides: A Versatile Class of Materials for Nitrogen Reduction Reactions. *Sci. China Mater.* **2022**, *65*, 2711−2720.
(23) Du, Z.; Wu, C.; Chen, Y.; Cao, Z.; Hu, R.; Zhang, Y.; Gu, J.; Cui, Y.; Chen, H.; Shi, Y.; Shang, J.; Li, B.; Yang, S. High-Entropy Atomic Layers of Transition-Metal Carbides (MXenes). *Adv. Mater.* **2021**, *33*, 2101473.
(24) Hu, J.; Cao, L.; Wang, Z.; Liu, J.; Zhang, J.; Cao, Y.; Lu, Z.; Cheng, H. Hollow High-Entropy Metal Organic Framework Derived Nanocomposite as Efficient Electrocatalyst for Oxygen Reduction Reaction. *Compos. Commun.* **2021**, *27*, 100866.
(25) Cao, S.; Li, Y.; Tang, Y.; Sun, Y.; Li, W.; Guo, X.; Yang, F.; Zhang, G.; Zhou, H.; Liu, Z.; Li, Q.; Shakouri, M.; Pang, H. Space-Confined Metal Ion Strategy for Carbon Materials Derived from Cobalt Benzimidazole Frameworks with High Desalination Performance in Simulated Seawater. *Adv. Mater.* **2023**, *35*, 2301011.
(26) Ma, Y.; Ma, Y.; Dreyer, S. L.; Wang, Q.; Wang, K.; Goonetilleke, D.; Omar, A.; Mikhailova, D.; Hahn, H.; Breitung, B.; Brezesinski, T. High-Entropy Metal-Organic Frameworks for Highly Reversible Sodium Storage. *Adv. Mater.* **2021**, *33*, 2101342.
(27) Ma, Y.; Hu, Y.; Pramudya, Y.; Diemant, T.; Wang, Q.; Goonetilleke, D.; Tang, Y.; Zhou, B.; Hahn, H.; Wenzel, W.; Fichtner, M.; Ma, Y.; Breitung, B.; Brezesinski, T. Resolving the Role of Configurational Entropy in Improving Cycling Performance of Multicomponent Hexacyanoferrate Cathodes for Sodium-Ion Batteries. *Adv. Funct. Mater.* **2022**, *32*, 2202372.
(28) Lun, Z.; Ouyang, B.; Kwon, D. H.; Ha, Y.; Foley, E. E.; Huang, T.; Cai, Z.; Kim, H.; Balasubramanian, M.; Sun, Y.; Huang, J.; Tian, Y.; Kim, H.; McCloskey, B. D.; Yang, W.; Clément, R. J.; Ji, H.; Ceder, G. Cation-Disordered Rocksalt-Type High-Entropy Cathodes for Li-Ion Batteries. *Nat. Mater.* **2021**, *20*, 214−221.
(29) Liu, Q.; Hu, Z.; Chen, M.; Zou, C.; Jin, H.; Wang, S.; Chou, S.; Liu, Y.; Dou, S. The Cathode Choice for Commercialization of Sodium-Ion Batteries: Layered Transition Metal Oxides versus Prussian Blue Analogs. *Adv. Funct. Mater.* **2020**, *30*, 1909530.
(30) Huang, J.; Li, Y.; Xie, R.; Li, J.; Tian, Z.; Chai, G.; Zhang, Y.; Lai, F.; He, G.; Liu, C.; Liu, T.; Brett, D. J. L. Structural Engineering of Cathodes for Improved Zn-Ion Batteries. *J. Energy Chem.* **2021**, *58*, 147−155.
(31) Kim, D. S.; Zakaria, M. B.; Park, M. S.; Alowasheeir, A.; Alshehri, S. M.; Yamauchi, Y.; Kim, H. Dual-Textured Prussian Blue Nanocubes as Sodium Ion Storage Materials. *Electrochim. Acta* **2017**, *240*, 300−306.
(32) Ma, X.; Jia, W.; Wang, J.; Zhou, J.; Wu, Y.; Wei, Y.; Zi, Z.; Dai, J. Synthesis of Copper Hexacyanoferrate Nanoflake as a Cathode for Sodium-Ion Batteries. *Ceram. Int.* **2019**, *45*, 740−746.
(33) Ren, W.; Qin, M.; Zhu, Z.; Yan, M.; Li, Q.; Zhang, L.; Liu, D.; Mai, L. Activation of Sodium Storage Sites in Prussian Blue Analogues via Surface Etching. *Nano Lett.* **2017**, *17*, 4713−4718.
(34) Liu, Y.; Qiao, Y.; Zhang, W.; Li, Z.; Ji, X.; Miao, L.; Yuan, L.; Hu, X.; Huang, Y. Sodium Storage in Na-Rich $Na_xFeFe(CN)_6$ Nanocubes. *Nano Energy* **2015**, *12*, 386−393.
(35) Zeng, Y.; Xu, J.; Wang, Y.; Li, S.; Luan, D.; Lou, X. D. Formation of CuMn Prussian Blue Analog Double-Shelled Nanoboxes Toward Long-Life Zn-ion Batteries. *Angew. Chem., Int. Ed.* **2022**, *61*, e202212031.
(36) Du, M.; Geng, P.; Pei, C.; Jiang, X.; Shan, Y.; Hu, W.; Ni, L.; Pang, H. High-Entropy Prussian Blue Analogues and Their Oxide Family as Sulfur Hosts for Lithium-Sulfur Batteries. *Angew. Chem., Int. Ed.* **2022**, *61*, e202209350.
(37) Wan, P.; Xie, H.; Zhang, N.; Zhu, S.; Wang, C.; Yu, Z.; Chu, W.; Song, L.; Wei, S. Stepwise Hollow Prussian Blue Nanoframes/Carbon Nanotubes Composite Film as Ultrahigh Rate Sodium Ion Cathode. *Adv. Funct. Mater.* **2020**, *30*, 2002624.
(38) Huang, Y.; Zhang, X.; Ji, L.; Wang, L.; Xu, B.; Shahzad, M. W.; Tang, Y.; Zhu, Y.; Yan, M.; Sun, G.; Jiang, Y. Boosting the Sodium Storage Performance of Prussian Blue Analogs by Single-Crystal and High-Entropy Approach. *Energy Storage Mater.* **2023**, *58*, 1−8.
(39) Shen, L.; Jiang, Y.; Liu, Y.; Ma, J.; Sun, T.; Zhu, N. High-Stability Monoclinic Nickel Hexacyanoferrate Cathode Materials for Ultrafast Aqueous Sodium Ion Battery. *Chem. Eng. J.* **2020**, *388*, 124228.
(40) Yu, H.; Fan, L.; Yan, H.; Deng, C.; Yan, L.; Shu, J.; Wang, Z. B. Nickel Ferrocyanides for Aqueous Ammonium Ion Batteries. *Inorg. Chem. Front.* **2022**, *9*, 2001−2010.
(41) Wang, L.; Lu, Y.; Liu, J.; Xu, M.; Cheng, J.; Zhang, D.; Goodenough, J. B. A Superior Low-Cost Cathode for a Na-Ion Battery. *Angew. Chem., Int. Ed.* **2013**, *52*, 1964−1967.
(42) Song, J.; Wang, L.; Lu, Y.; Liu, J.; Guo, B.; Xiao, P.; Lee, J.; Yang, X.; Henkelman, G.; Goodenough, J. B. Removal of Interstitial H_2O in Hexacyanometallates for a Superior Cathode of a Sodium-Ion Battery. *J. Am. Chem. Soc.* **2015**, *137*, 2658−2664.
(43) Zuo, D.; Wang, C.; Han, J.; Wu, J.; Qiu, H.; Zhang, Q.; Lu, Y.; Lin, Y.; Liu, X. Oriented Formation of a Prussian Blue Nanoflower as a High Performance Cathode for Sodium Ion Batteries. *Acs Sustain. Chem. Eng.* **2020**, *8*, 16229−16240.
(44) Zhang, W.; Zhao, Y.; Malgras, V.; Ji, Q.; Jiang, D.; Qi, R.; Ariga, K.; Yamauchi, Y.; Liu, J.; Jiang, J.; Hu, M. Synthesis of Monocrystalline Nanoframes of Prussian Blue Analogues by Controlled Preferential Etching. *Angew. Chem., Int. Ed.* **2016**, *55*, 8228−8234.
(45) Shang, Y.; Li, X.; Song, J.; Huang, S.; Yang, Z.; Xu, Z. J.; Yang, H. Unconventional Mn Vacancies in Mn-Fe Prussian Blue Analogs: Suppressing Jahn-Teller Distortion for Ultrastable Sodium Storage. *Chem* **2020**, *6*, 1804−1818.
(46) Issa, B.; Obaidat, I.; Albiss, B.; Haik, Y. Magnetic Nanoparticles: Surface Effects and Properties Related to Biomedicine Applications. *Int. J. Mol. Sci.* **2013**, *14*, 21266−21305.
(47) Ren, W.; Yao, X.; Niu, C.; Zheng, Z.; Zhao, K.; An, Q.; Wei, Q.; Yan, M.; Zhang, L.; Mai, L. Cathodic Polarization Suppressed Sodium-Ion Full Cell with a 3.3 V High-Voltage. *Nano Energy* **2016**, *28*, 216−223.
(48) Yu, H.; Wang, Z.; Zheng, R.; Yan, L.; Zhang, L.; Shu, J. Toward Sustainable Metal-Iodine Batteries: Materials, Electrochemistry and Design Strategies. *Angew. Chem., Int. Ed.* **2023**, *62*, 202308397.
(49) Yao, Y.; McDowell, M. T.; Ryu, I.; Wu, H.; Liu, N.; Hu, L.; Nix, W. D.; Cui, Y. Interconnected Silicon Hollow Nanospheres for Lithium-Ion Battery Anodes with Long Cycle Life. *Nano Letters* **2011**, *11*, 2949−2954.
(50) Zeng, Y.; Lu, X.; Zhang, S.; Luan, D.; Li, S.; Lou, X. Construction of Co-Mn Prussian Blue Analog Hollow Spheres for Efficient Aqueous Zn-ion Batteries. *Angew. Chem., Int. Ed.* **2021**, *60*, 22189−22194.
(51) Zhang, L.; Zhang, M.; Guo, H.; Tian, Z.; Ge, L.; He, G.; Huang, J.; Wang, J.; Liu, T.; Parkin, I. P.; Lai, F. A Universal Polyiodide Regulation Using Quaternization Engineering toward

High Value-Added and Ultra-Stable Zinc-Iodine Batteries. *Adv. Sci.* **2022**, *9*, 2105598.
(52) Chen, M.; Zhu, W.; Guo, H.; Tian, Z.; Zhang, L.; Wang, J.; Liu, T.; Lai, F.; Huang, J. Tightly Confined Iodine in Surface-Oxidized Carbon Matrix Toward Dual-Mechanism Zinc-Iodine Batteries. *Energy Storage Mater.* **2023**, *59*, 102760.
(53) Yu, Z.; Cheng, H.; Lyu, Y.; Liu, Y.; Zhou, J.; Chen, R.; Guo, B. A Vacancy-Free Sodium Manganese Hexacyanoferrate as Cathode for Sodium-Ion Battery by High-Salt-Concentration Preparation. *J. Alloys Compd.* **2021**, *887*, 161388.
(54) Brezesinski, T.; Wang, J.; Tolbert, S. H.; Dunn, B. Ordered Mesoporous Alpha-MoO_3 with Iso-Oriented Nanocrystalline Walls for Thin-Film Pseudocapacitors. *Nat. Mater.* **2010**, *9*, 146−151.
(55) An, Q.; Li, Y.; Yoo, H. D.; Chen, S.; Ru, Q.; Mai, L.; Yao, Y. Graphene Decorated Vanadium Oxide Nanowire Aerogel for Long-Cycle-Life Magnesium Battery Cathodes. *Nano Energy* **2015**, *18*, 265−272.
(56) Rizvandi, O. B.; Yesilyurt, S. Modeling and Performance Analysis of Branched Microfluidic Fuel Cells with High Utilization. *Electrochim. Acta* **2019**, *318*, 169−180.

https://doi.org/10.1021/acsami.4c04785
ACS Appl. Mater. Interfaces 2024, 16, 27684−27693